Wu et al. *Quantum Frontiers* (2023) 2:17
https://doi.org/10.1007/s44214-023-00042-0

Quantum Frontiers
上海交通大學 SHANGHAI JIAO TONG UNIVERSITY 李政道研究所 Tsung-Dao Lee Institute

ORIGINAL ARTICLE Open Access

Topological magnetic line defects in Fe(Te, Se) high-temperature superconductors

Xianxin Wu[1*], Jia-Xin Yin[2,3], Chao-Xing Liu[4*] and Jiangping Hu[5,6*]

Abstract

The realization of Majorana zero modes in condensed matter have been attracting enormous interests from fundamental science such as topological quantum computation. Recently iron based superconductors were identified as a high-temperature platform for realizing topological superconductivity and Majorana modes. As unconventional superconductors, one of the most important characteristics of them is that they are in the vicinity of magnetic states due to the strong Hund's coupling in iron atoms. Here we propose that the line defects with missing Te/Se anions in Fe(Se, Te) superconductors provide the realization of intrinsic antiferromagnetic (AFM) chains with Rashba spin-orbit coupling. Against conventional wisdom, Majorana zero modes (MZMs) can be robustly generated at these AFM chain ends. These results can consistently explain the recent experimental observation of zero-energy end states in line defects of monolayer Fe(Te, Se)/$SrTiO_3$ by scanning tunneling microscopy (STM) measurements. Our research not only demonstrates an unprecedented interplay among native line defect, emergent magnetism and topological superconductivity but also explores a high-temperature platform for Majorana fermions.

1 Introduction

Majorana zero modes, hosted in the surface or edge of topological superconductors, have drawn enormous attentions in condensed matter physics, due to its non-Abelian statistics, which is essential for fault-tolerant quantum computation [1–9]. There have been many studies including both theoretical proposals [10–19] and experimental efforts [20–27] for their realization. In particular, a ferromagnetic atomic chain on an *s*-wave superconducting substrate [22] has been experimentally shown to generate MZMs at its ends, where the spin-polarized bands are forced to favor *p*-wave pairing. However, there is little investigation along the other way of thinking, namely, searching for superconductors with intrinsic magnetic chains. As conventional superconductors are incompatible with magnetism, unconventional superconductors are promising candidates.

Recently, theoretical predictions and experimental measurements have identified topological band structures in some families of iron-based superconductors [28–36]. The natural integration of topological properties and high T_c superconductivity in iron based superconductors have rendered them an exciting platform to realize topological superconductivity at high temperature. MZMs localized in impurities or vortex cores are evidenced by the zero-bias peaks in STM experiments in both iron chalcogenides (Fe(Te, Se) crystals) and iron pnictides ($CaKFe_4As_4$) [37–43]. In addition, in two-dimensional (2D) monolayer $FeSe_{1-x}Te_x/SrTiO_3$ (STO), the band inversion process at Γ point has been directly observed with increasing x and the system becomes topologically nontrivial when $x > 0.79$ [35, 36]. Based on discovered topological band structures, high-order topological superconductivity with Majorana hinge/corner states has been proposed to be realized in iron based superconductors as well [44–49].

Besides the topological properties, one of the most prominent features for iron-based superconductors, dis-

*Correspondence: xxwu@itp.ac.cn; cxl56@psu.edu; jphu@iphy.ac.cn
[1]CAS Key Laboratory of Theoretical Physics, Institute of Theoretical Physics, Chinese Academy of Sciences, Beijing 100190, China
[4]Department of Physics, The Pennsylvania State University, University Park, PA, 16802, USA
Full list of author information is available at the end of the article

tinct from conventional superconductors, is that they are in a vicinity of magnetic order states owing to the strong Hund's coupling in iron atoms. Despite an isolated Fe atom has a large magnetic moment, in the crystals of Fe-based superconductors, electrons of Fe atoms become delocalized through hybridizations with anions, suppressing local magnetic moments. Thus, in the absence of or by weakening the anion bridging, Fe atoms have a tendency towards strong local magnetism. Line defects formed by missing anions have been observed recently in a monolayer $FeTe_{0.5}Se_{0.5}$/STO [50]. Surprisingly, a zero-bias peak at the ends of atomic line defects was detected, highly resembling the characteristics of MZMs [50]. Considering the magnetic nature of Fe atoms, it is naturally to conjecture that the line defects may be new platforms for high-temperature MZMs.

In this work, we study the electronic properties of these line defects formed by missing Se/Te anions in Fe(Se, Te) monolayer to explore their topological nature. Our first-principles calculations reveal that the d_{yz} and $d_{x^2-y^2}$ orbitals of Fe atoms in the line defect contribute to flat bands near the Fermi level, leading to a magnetic instability. Further calculations suggest an AFM configuration is energetically more favorable, in sharp contrast to the hypothetical nonmagnetic nature. In both ferromagnetic(FM) and AFM configurations, d_{xz} bands are partially occupied and dominantly contribute to Fermi surfaces. By including Rashba spin-orbit coupling (SOC), an odd number of 1D bands cross the Fermi level in the magnetic states and the underlying intrinsic superconductivity in Fe(Se, Te) drives the line defect into a 1D topological superconducting phase with MZMs at its ends. To our knowledge, this is the first realistic instance of realizing MZMs in an AFM chain. Owing to the compatibility of superconductivity and antiferromagnetism, our study suggests that the missing anion magnetic line defects provide a unique platform to explore AFM topological superconductivity and MZMs.

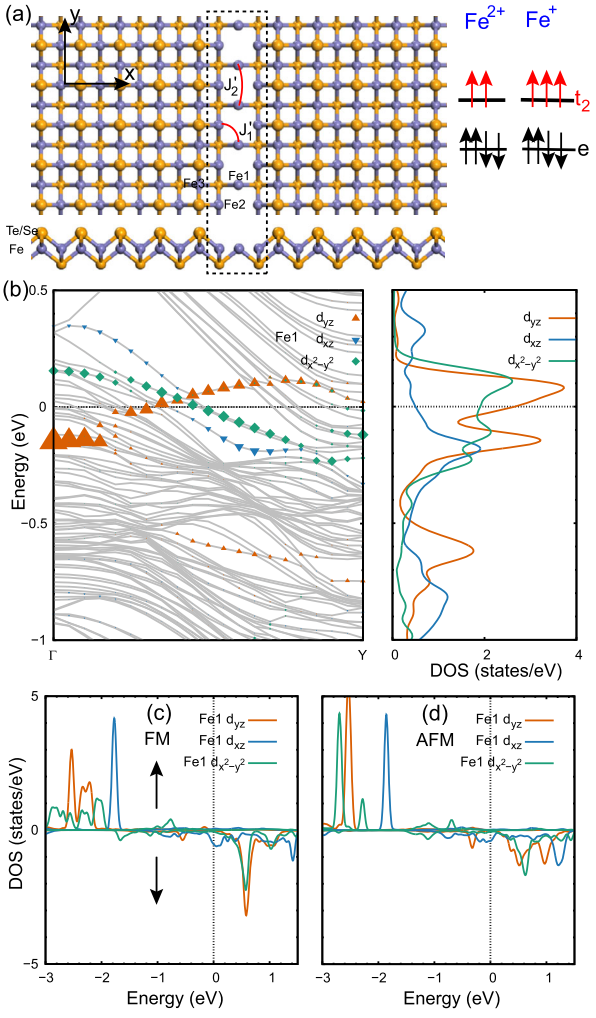

Figure 1 *Crystal structure and electronic structures for the line defect in monolayer Fe(Te, Se)/STO.* (a) A schematic of the line defects in monolayer Fe(Te, Se)/STO and occupations of Fe^{2+} and Fe^+ 3*d* electrons in tetrahedral coordination environments. (b) Band structure and DOS for the line defects in monolayer FeSe. Spin-resolved DOS for a Fe1 atom in the FM (c) and AFM (d) configurations. The sizes of triangles and diamonds represent the orbital weight of iron atoms Fe1 in the line defect

2 Result

Band structure for line defects in monolayer Fe(Te, Se)

The line defect in monolayer Fe(Te, Se), displayed in Fig. 1(a), corresponds to a line missing of top Te/Se atoms, naturally emerging in the growth process [50]. Compared with normal Fe atoms in Fe(Te, Se), the iron atoms Fe1 in the defect can only couple with two nearest Te/Se atoms, which should generate a significant change in the local electronic structure.

We perform first-principles calculations to study the electronic structure for the line defect and the details can be found in Sect. I of supplementary materials (SM) (Additional file 1). In the following, we discuss the line defect in monolayer FeSe in our calculations, as the atomic relaxation and the substitution of Te for Se will not qualitatively change the results (see Sect. I in SM). Due to the tetrahedral crystal field in iron based superconductors, the five *d* orbitals of iron are split into t_2 and *e* orbitals. In Fe(Te, Se) systems, iron atoms have a nominal valence of Fe^{2+} and *e* orbitals are occupied while t_2 orbital are partially filled, contributing dominantly to the Fermi surfaces. However, the absence of top Te/Se atoms in the line defect will change the valence of the corresponding iron atoms Fe1, which are expected to have a nominal $3d^7$ (Fe^+) configuration. Figure 1(b) displays the band structure and density of states for a line defect in monolayer FeSe, where the gray lines denote the bulk bands and the lines with triangles and squares are bands from the line defect. We notice that the

t_2 orbitals of Fe1, including d_{xz}, d_{yz} and $d_{x^2-y^2}$, are nearly half-filled, consistent with occupations of Fe^+ $3d$ electrons. Moreover, the most prominent feature is that the d_{yz} and $d_{x^2-y^2}$ bands of Fe1 are extremely flat, in sharp contrast to the normal Fe bands. These flat bands originate from the reduced hopping along y direction due to the missing line Te/Se atoms, contributing a large density of states (DOS) near the Fermi level, as displayed in Fig. 1(b). By comparing the DOS of Fe atoms close to the line defect (see Sect. I in SM), we find that the DOS at the Fermi level $D(E_f)$ of Fe atoms in the line defect is almost two times larger than that of bulk Fe. This large $D(E_f)$ is relatively robust against electron doping in the realistic monolayer Fe(Te, Se)/STO. According to the Stoner criterion, a large $D(E_f)$ can induce a magnetic instability if interactions are sufficiently strong.

Magnetic configurations of line defects We turn to investigate the magnetic order and the corresponding electronic structures of line defects in monolayer Fe(Te, Se). The magnetic order in iron chalcogenides can be described by a Heisenberg model with the nearest, the next-nearest, and the next next-nearest neighbor couplings J_1, J_2, and J_3 [51]. All of them have a superexchange origin mediated by Te/Se hence are antiferromagnetic. As a consequence, the absence of top Te/Se atoms in the line defect will significantly reduce the corresponding exchange coupling between nearest and next-nearest neighbor Fe1 atoms and we label these exchange couplings as J_1' and J_2', as depicted in Fig. 1(a). For Fe1 with half-filled t_2 orbitals, J_2' is derived from the direct exchange coupling and should be antiferromagnetic.

For this one-dimensional (1D) line defect, we only consider FM and AFM configurations and neglect complicated spiral magnetic orders due to the short-ranged exchange couplings. In the FM configuration, the antiferromagnetic J_1' can induce a small opposite magnetic moment on Fe2 with respect to Fe1 (see Sect. I in SM). The magnetic states of the defect can be described by a Heisenberg model with nearest neighbor coupling J_{eff},

$$H = \sum_{\langle ij \rangle} J_{eff} \boldsymbol{S}_{1i} \cdot \boldsymbol{S}_{1j}, \tag{1}$$

where $\boldsymbol{S}_{1i}$ is the magnetic moment for Fe1 and J_{eff} includes contributions from the direct coupling J_2' and indirect coupling J_1'. As J_1' effectively contributes a ferromagnetic coupling between nearest neighbor iron atoms, the J_1' coupling will compete with J_2' term. The corresponding energies per Fe for FM and AFM states based on the above Heisenberg model are: $E_{FM} = -4J_1'S_1S_2 + J_2'S_1^2$, $E_{AFM} = -J_2'S_1^2$, where S_1 (S_2) is the magnetic moment for iron atoms Fe1 (Fe2) in the line defect. The line defect favors a FM order if $J_2'/J_1' < 2S_2/S_1$ otherwise an AFM order. According to our calculation, the magnetic states have a much lower energy compared with the nonmagnetic state (about 1 eV/Fe) and $S_2/S_1 \sim 0.1$ in the FM state. Moreover, the AFM configuration is 13 meV/Fe lower in energy than the FM configuration, leading to $J_{eff} = 6.5$ meV/S_1^2, where the magnetic moment of Fe1 is about 2.9 μ_B, close to the value for half-filled t_2 orbitals. The easy axis of the Fe spin moments is out-of-plane (z axis in Fig. 1) and about 1.7 meV/Fe lower in energy than the two high-symmetry in-plane directions.

In the FM state, the DOS for Fe1 atoms is shown in Fig. 1(c), where majority-spin t_2 orbital are occupied while the minority-spin d_{xz} band is partially filled, contributing two Fermi points around Y (see Sect. I in SM). In the AFM state, each band is two-fold degenerate without including SOC, the minority-spin d_{xz} band of one Fe1 is partially occupied, as shown in Fig. 1(d), and there are Fermi points around Y (see Sect. I in SM). In both cases, d_{xz} orbitals dominate the Fermi points for the line defects.

Majorana modes at the ends of line defects From our above calculations, we find that the line defects in monolayer Fe(Te, Se) are intrinsically magnetic. Although the energy of AFM configuration is slightly lower than that of FM configuration, we consider both configurations in the following model calculations. The 1D line defect can be theoretically described by the Hamiltonian,

$$\begin{aligned}
\mathcal{H}_{LD} = & \sum_{ij\alpha\sigma} \left[t_{\alpha,ij}\delta_{\langle ij \rangle} + (\epsilon_\alpha - \mu)\delta_{ij} \right] c^\dagger_{i\alpha\sigma} c_{j\alpha\sigma} \\
& + \sum_{\langle ij \rangle \sigma} \left(t_{23} c^\dagger_{i2\sigma} c_{j3\sigma} + h.c. \right) \\
& + \sum_{i\alpha\sigma_1\sigma_2} \frac{1}{2} \boldsymbol{M}_{i\alpha} \cdot \boldsymbol{s}_{\sigma_1\sigma_2} c^\dagger_{i\alpha\sigma_1} c_{i\alpha\sigma_2} \\
& + \sum_{\langle ij \rangle \alpha} \left[i\lambda_R \left(c^\dagger_{i\alpha\uparrow} c_{j\alpha\downarrow} + c^\dagger_{i\alpha\downarrow} c_{j\alpha\uparrow} \right) + h.c. \right] \\
& + \sum_{ij\alpha\sigma} \left[\sigma (\Delta_0 \delta_{ij} + \Delta_1 \delta_{\langle ij \rangle}) c^\dagger_{i\alpha\sigma} c^\dagger_{j\alpha\bar{\sigma}} + h.c. \right],
\end{aligned} \tag{2}$$

where $\langle ij \rangle$ labels the nearest neighbor Fe1 sites, $\alpha = 1, 2, 3$ represent d_{xz}, d_{yz} and $d_{x^2-y^2}$ orbitals for iron atoms in the line defect and s_i labels the Pauli matrix in spin space. The first and second term are the kinetic energy part, where the d_{xz} orbital is decoupled from the other two due to the mirror reflection with respect to the line defect. The third term describes the magnetic coupling for each iron site. This magnetic coupling is assumed to be orbital independent and can be expressed as $\boldsymbol{M}_{i\alpha} = \boldsymbol{m}_0 + (-1)^i \boldsymbol{m}_1$, where $\boldsymbol{m}_0$ ($\boldsymbol{m}_1$) is the FM (AFM) coupling. The fourth term is the Rashba SOC due to the mirror symmetry breaking from the absence of top Se/Te atoms and a built-in electric field induced by the charge transfer from STO to monolayer

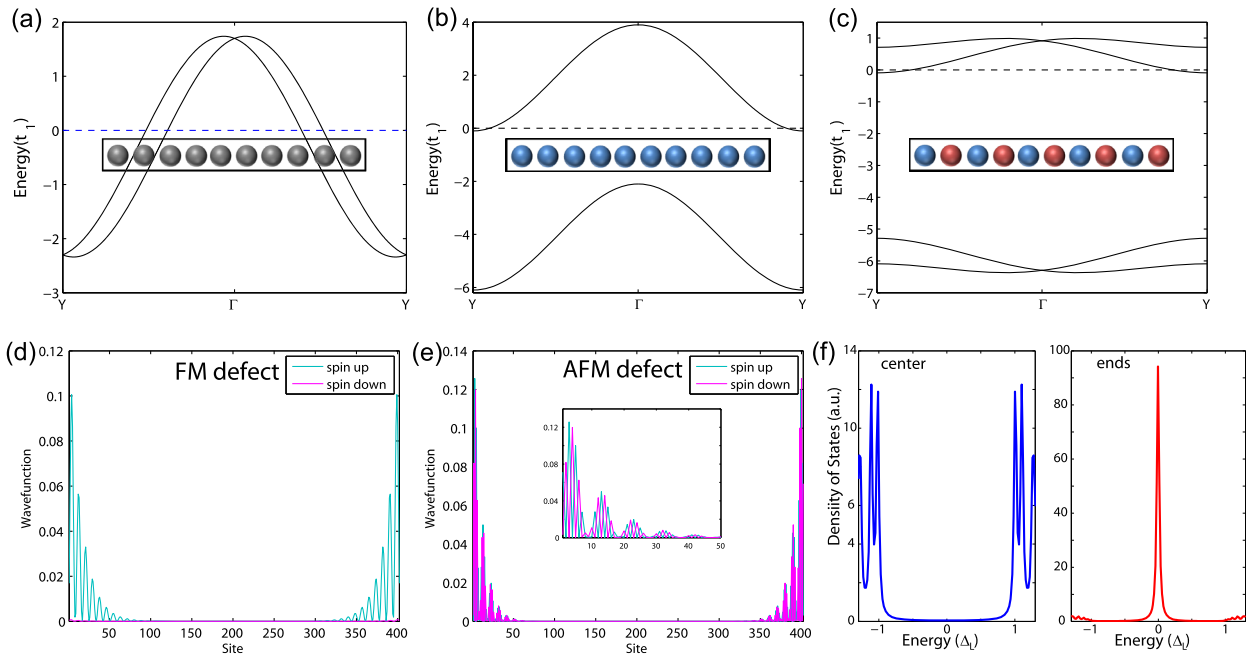

Figure 2 *Band structures in one-band model with Rashba SOC and magnetic couplings and Majorana profiles and local DOS on the line defect.* Band structures in normal states for the line defect with nonmagnetic (a), FM (b) and AFM (c) states. The spin-resolved wavefunctions of MZMs in the FM (d) and AFM (e) line defects. (f) Local DOS at the center and ends of the AFM line defect including superconductivity with open boundary condition. The electron filling is $n = 1.1$ per site and we adopt $\lambda_R = 0.2t_1$ and $\boldsymbol{m}_0 = 6t_1\hat{\boldsymbol{z}}$ ($\boldsymbol{m}_1 = 6t_1\hat{\boldsymbol{z}}$) for the FM (AFM) line defect. Δ_L is the effective pairing gap for the band crossing the Fermi level in AFM line defects and $\Delta_L = 0.025$ with $\Delta_0 = 0.12$ and $\Delta_1 = 0$

Fe(Te, Se) [52], which is sizable in first-principles calculations (see Sect. I in SM) and crucial for topological superconductivity in the AFM configuration. The last term describes the onsite and nearest neighbor spin singlet pairing in proximity to the superconducting monolayer Fe(Te, Se) and the orbital independent pairing is adopted for convenience. By fitting to the band structure in Fig. 1(b), the hopping parameters are $t_1 = 0.15$, $t_2 = -0.065$, $t_3 = 0.09$ and $t_{23} = 0.004$ eV.

The band structures from the above model in nonmagnetic and FM states are qualitatively consistent with first-principles calculations in both configurations (see Sect. I in SM). Since the Fermi points in normal states are predominantly attributed to d_{xz} orbitals in magnetic states (see Fig. 1(c) and (d)), we can further simplify the above model to a single-orbital one. Then, the Bogoliubov-de Gennes (BdG) Hamiltonian can be written as $\mathcal{H}^1_{LD} = \sum_{\boldsymbol{k}} \Psi^\dagger_{\boldsymbol{k}} h_{LD}(\mathbf{k}) \Psi_{\boldsymbol{k}}$, with the basis being $\Psi^\dagger_{\boldsymbol{k}} = (\psi^\dagger_{\boldsymbol{k}}, \psi^T_{-\boldsymbol{k}})$ and $\psi^\dagger_{\boldsymbol{k}\sigma} = (c^\dagger_{\boldsymbol{k}a\uparrow}, c^\dagger_{\boldsymbol{k}b\uparrow}, c^\dagger_{\boldsymbol{k}a\downarrow}, c^\dagger_{\boldsymbol{k}b\downarrow})$, where a, b is the sublattice index of Fe1 site. The Hamiltonian matrix reads,

$$h_{LD}(\boldsymbol{k}) = 2t_1 \cos\frac{k}{2}\tau_z\sigma_x - 2\lambda_R \sin\frac{k}{2}\tau_0 s_x\sigma_x + \frac{m_0}{2}\tau_z s_z + \frac{m_1}{2}\tau_z s_z\sigma_z + \mu\tau_z - \Delta_0'\tau_y s_y\sigma_0 - \Delta_0''\tau_x s_y\sigma_0 - \Delta_1'\tau_y s_y\sigma_x - \Delta_1''\tau_x s_y\sigma_x, \quad (3)$$

where $\boldsymbol{\sigma}$ and $\boldsymbol{\tau}$ label the Pauli matrices in the sublattice and Nambu spaces and $\Delta'_{0/1}$ and $\Delta''_{0/1}$ are the real and imaginary parts of the superconducting pairing $\Delta_{0/1}$, respectively. Generally the above Hamiltonian has the particle-hole symmetry $\mathcal{C}h_{LD}(\boldsymbol{k})\mathcal{C}^{-1} = -h_{LD}(-\boldsymbol{k})$ with $\mathcal{C} = \tau_x\mathcal{K}$ and $\mathcal{K}$ being the complex conjugate operation, belonging to symmetry class D.

Without magnetic orders, the representative band structure in normal states is shown in Fig. 2(a), where time reversal symmetry protects a degeneracy at $k = 0, \pi$ and the Fermi level always crosses even number of bands. In the FM state, the bands are non-degenerate and only one minority-spin band crosses the Fermi level, contributing two Fermi points around Y, as shown in Fig. 2(b). As the electron pockets of monolayer Fe(Te, Se) are projected to Y point in line defects, these Fermi points will obtain a superconducting gap by proximity effect. Most importantly, the effective pairing is p-wave as required by the Fermionic antisymmetry, resembling to the 1D Kitaev model [5]. Due to the nontrivial topology, the system remains gapped in the center while two MZMs will occur at the ends of the line defect (see Sect. II in SM).

In the AFM state, there is an effective time reversal symmetry $\tilde{\Theta} = \Theta T_{\frac{1}{2}}$, combining time reversal symmetry Θ and a half-lattice translation $T_{\frac{1}{2}}$. $\tilde{\Theta}^2 = \mp 1$ at $k = 0, \pi$ suggests that Kramers degeneracy only occurs at $k = 0$ but not $k = \pi$. At a generic k point, the intrinsic Rashba SOC lifts the degeneracy. In contrast to the Rashba band of a nanowire, the prominent feature is that an odd number of 1D bands cross the Fermi level in a wide range of chemical potential. When the exchange coupling m_1 is relatively strong (see Fig. 1(c) and (d)), the representative band structure is displayed in Fig. 2(c) and only one band with mixed minority-spin and majority-spin contributions cross the Fermi level. Further including superconductivity, it naturally induces MZMs located at the ends of the line defect, displayed in Fig. 2 (f). We emphasize that there is only one MZM at each end, distinct from the topological Shockley defect scenario [50, 53]. Figure 2(d) and (e) display the spin-resolved spatial profiles of MZMs in FM and AFM line defects. The MZMs are localized at ends in both cases but the spin polarization of MZMs differs. In the former, there is a uniform spin polarization, however, in the latter, the spin polarization is spatially alternating.

The phase diagram of topological superconductivity in line defect as a function of AFM and FM couplings is displayed in Fig. 3(a). In the region I, an odd number of bands cross the Fermi level, inducing a topological phase. Furthermore, the m_1-dominated region is much larger than the m_0-dominated one, suggesting that AFM line defect is easier for the realization of MZMs. In the region II, there are an even number of bands crossing the Fermi level and the system is generally topologically trivial in the class D, where the topological invariant is $\mathbb{Z}_2$ in 1D. The m_0-dominated and m_1-dominated phases are always separated by a trivial from a band analysis (see Sect. II in SM). If an increasing external magnetic field can induce a phase transition from an AFM state to a FM state, it could also render topological phase transitions first from a nontrivial phase to a trivial one then back to a nontrivial one. The corresponding local DOS evolution at ends of line defects can be found in Sect. II of SM.

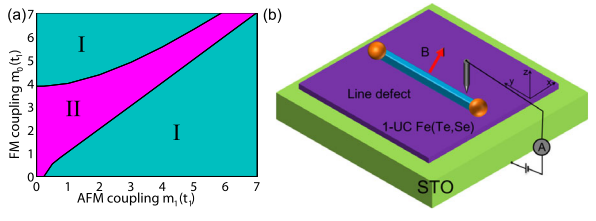

Figure 3 *Phase diagram and experimental setup.* (a) Phase diagram for topological superconductivity of line defect as a function of AFM and FM couplings. In region I (II), an odd (even) number of 1D bands cross the Fermi level, resulting a topologically nontrival (trivial) phase. The electron filling is $n = 1.1$ per site and we adopt $\lambda_R = 0.2t_1$ and the exchange field is perpendicular to the line defect(along z direction). (b) The schematic for experimentally distinguishing topological Shockley defects, AFM and FM scenarios

3 Discussion

Our results are distinct from those in Ref. [50, 53], where MZMs are considered as a Kramers pair in topological Shockley defects protected by time-reversal symmetry. These two different schemes can be distinguished by applying an external magnetic field. In the Shockley case, once the time-reversal symmetry is broken by an external magnetic field parallel to the Rashba spin-orbit field (along x axis in Fig. 3(b)), the Krammers pair of MZM will split (see Sect. III in SM). In our case, however, there is only one MZM at each end of the magnetic line defect and it is robust against weak external perturbations.

As long as an odd number of bands acquire the proximity superconducting gap, the line defect is topological, regardless of the pairing symmetry of monolayer Fe(Te, Se). The scenario of the AFM line defects is consistent with available experimental evidences. The observed in-gap bound states on a single Te/Se vacancy defect in monolayer Fe(Te, Se)/STO are reminiscent of the Yu-Shiba-Rusinov (YSR) states in superconductors [50], indicating its magnetic nature. If the line defect is FM, it can be considered as magnetic impurities in Fe(Te, Se) superconductors and thus YSR ingap states are also expected. However, there are no other in-gap states except zero-energy end states on the line defect in STM measurements [50]. In contrast, as the total magnetization of an AFM line defect vanishes, it performs as a nonmagnetic impurity and therefore there are no in-gap states, consistent with STM measurements. Moreover, the effective superconducting gap for the line defect is proportional to the Rashba SOC strength in the FM state and is expected to be much smaller than the bulk superconducting gap. On the contrary, the nearest-neighbor pairing is allowed in the AFM state and the SC gap should be comparable to the bulk value, in agreement with experiments [50].

To experimentally distinguish AFM and FM scenarios shown in Fig. 3(b), spin-polarized STM measure can provide direct evidence about the magnetic nature of line defects and the spin-resolved spatial profiles of MZMs at ends, as depicted in Fig. 2(d) and (e). Moreover, MZMs in the two cases will exhibit distinct behaviors under an external magnetic field $\boldsymbol{B}$ along the magnetization axis: the MZMs are robust in FM line defects; however, for AFM line defects, a large magnetic field drives topological phase transitions and the zero-bias peak at ends will first split at certain $\boldsymbol{B}$ and emerge again at a larger $\boldsymbol{B}$ (see Sect. II in SM).

Conclusion We study the topological superconductivity of intrinsic line defects in monolayer Fe(Te, Se)/$SrTiO_3$. First-principles calculations reveal that the missing Te/Se

atoms introduce a large DOS near the Fermi level, inducing a magnetic order on the line defect. In either FM or AFM configurations, the line defect is 1D topologically superconducting, which hosts MZMs at its ends, consistent with recent STM experiments. In particular, we find the AFM configuration is energetically more favorable and the MZMs in the AFM configuration has a spatially alternating spin-polarized profile. The AFM line defects, derived from atomic vacancies, are quite common and almost unavoidable and can also occur in iron pnictides, cuprates or other superconducting materials. As superconductivity and antiferromagnetism are compatible, they offer a novel and concise platform to explore AFM topological superconductivity and realize MZMs.

4 Methods

Our DFT calculations employ the projector augmented wave (PAW) method encoded in the Vienna *ab initio* simulation package (VASP) [54–56], and the generalized-gradient approximation (GGA) [57] for the exchange correlation functional are used. The cutoff energy of 500 eV is taken for expanding the wave functions into plane-wave basis. In the calculation for the line defect, the Brillouin zone is sampled in the k space within the Monkhorst-Pack scheme [58]. The number of these k points is $1 \times 11 \times 1$ for monolayer FeSe and FeTe. In the calculations, the inplane lattice constant a = 3.905 Å and the height of the Se/Te anions from the Fe plane h = 1.50 Å are adopted [36]. To model a line defect in Fe(Te, Se), we choose a 15×1 supercell of monolayer FeSe with a vacuum layer of 25 Å along z direction and remove one top Se atom in the center. This slab is large enough to avoid interactions between the adjacent line defects. We also study the effect of atomic relaxation and the substitution of Te for Se in monolayer FeSe on the band structure with a 7×1 supercell, where internal atomic positions and forces are minimized to less than 0.02 eV/Å.

Supplementary information

Supplementary information accompanies this paper at https://doi.org/10.1007/s44214-023-00042-0.

Additional file 1. (PDF 4.7 MB)

Funding

Open access funding provided by Shanghai Jiao Tong University. X. Wu was supported by the National Natural Science Foundation of China (grant no. 12047503). J. Hu was supported by the Ministry of Science and Technology (grant no. 2022YFA1403901), the National Natural Science Foundation of China (grant no. NSFC-11888101) and the New Cornerstone Foundation.

Availability of data and materials

The data that support the findings of this study are available from the first author upon reasonable request.

Declarations

Competing interests

The authors declare no competing interests.

Author contributions

XW, CL and JH conceived this project. XW performed the numerical calculations and XW, JY, CL and JH performed the analysis. XW, CL and JH wrote the manuscript and all the authors participated in the discussion. All authors read and approved the final manuscript.

Author details

[1]CAS Key Laboratory of Theoretical Physics, Institute of Theoretical Physics, Chinese Academy of Sciences, Beijing 100190, China. [2]Department of Physics, Southern University of Science and Technology, Shenzhen, Guangdong, China. [3]Quantum Science Center of Guangdong-Hong Kong-Macao Greater Bay Area (Guangdong), Shenzhen, China. [4]Department of Physics, The Pennsylvania State University, University Park, PA, 16802, USA. [5]Beijing National Laboratory for Condensed Matter Physics, and Institute of Physics, Chinese Academy of Sciences, Beijing 100190, China. [6]CAS Center of Excellence in Topological Quantum Computation and Kavli Institute of Theoretical Sciences, University of Chinese Academy of Sciences, Beijing 100190, China.

Received: 28 September 2023 Revised: 12 November 2023
Accepted: 13 November 2023 Published online: 27 November 2023

References

1. Ivanov DA (2001) Non-Abelian statistics of half-quantum vortices in *p*-wave superconductors. Phys Rev Lett 86:268–271
2. Kitaev AY (2003) Fault-tolerant quantum computation by anyons. Ann Phys 303:2–30
3. Kitaev A (2006) Anyons in an exactly solved model and beyond. Ann Phys 321:2–111
4. Nayak C, Simon SH, Stern A, Freedman M, Das Sarma S (2008) Non-Abelian anyons and topological quantum computation. Rev Mod Phys 80:1083–1159
5. Alicea J (2012) New directions in the pursuit of Majorana fermions in solid state systems. Rep Prog Phys 75:076501
6. Sarma SD, Freedman M, Nayak C (2015) Majorana zero modes and topological quantum computation. npj Quantum Inf 1:15001
7. Aasen D et al (2016) Milestones toward Majorana-based quantum computing. Phys Rev X 6:031016
8. Elliott SR, Franz M (2015) Colloquium: Majorana fermions in nuclear, particle, and solid-state physics. Rev Mod Phys 87:137–163
9. Karzig T et al (2017) Scalable designs for quasiparticle-poisoning-protected topological quantum computation with Majorana zero modes. Phys Rev B 95:235305
10. Rice TM, Sigrist M (1995) Sr_2RuO_4: an electronic analogue of 3He? J Phys Condens Matter 7:L643–L648
11. Das Sarma S, Nayak C, Tewari S (2006) Proposal to stabilize and detect half-quantum vortices in strontium ruthenate thin films: non-Abelian braiding statistics of vortices in a $p_x + ip_y$ superconductor. Phys Rev B 73:220502
12. Fu L, Kane CL (2008) Superconducting proximity effect and Majorana fermions at the surface of a topological insulator. Phys Rev Lett 100:096407
13. Lutchyn RM, Sau JD, Das Sarma S (2010) Majorana fermions and a topological phase transition in semiconductor-superconductor heterostructures. Phys Rev Lett 105:077001
14. Oreg Y, Refael G, von Oppen F (2010) Helical liquids and Majorana bound states in quantum wires. Phys Rev Lett 105:177002
15. Sau JD, Lutchyn RM, Tewari S, Das Sarma S (2010) Generic new platform for topological quantum computation using semiconductor heterostructures. Phys Rev Lett 104:040502
16. Alicea J (2010) Majorana fermions in a tunable semiconductor device. Phys Rev B 81:125318
17. Nadj-Perge S, Drozdov IK, Bernevig BA, Yazdani A (2013) Proposal for realizing Majorana fermions in chains of magnetic atoms on a superconductor. Phys Rev B 88:020407
18. Braunecker B, Simon P (2013) Interplay between classical magnetic moments and superconductivity in quantum one-dimensional conductors: toward a self-sustained topological Majorana phase. Phys Rev Lett 111:147202

19. Klinovaja J, Stano P, Yazdani A, Loss D (2013) Topological superconductivity and Majorana fermions in RKKY systems. Phys Rev Lett 111:186805
20. Mourik V et al (2012) Signatures of Majorana fermions in hybrid superconductor-semiconductor nanowire devices. Science 336:1003
21. Wang M-X et al (2012) The coexistence of superconductivity and topological order in the Bi_2Se_3 thin films. Science 336:52
22. Nadj-Perge S et al (2014) Observation of Majorana fermions in ferromagnetic atomic chains on a superconductor. Science 346:602–607
23. Sun H-H et al (2016) Majorana zero mode detected with spin selective Andreev reflection in the vortex of a topological superconductor. Phys Rev Lett 116:257003
24. Deng MT et al (2016) Majorana bound state in a coupled quantum-dot hybrid-nanowire system. Science 354:1557
25. Pawlak R et al (2016) Probing atomic structure and Majorana wavefunctions in mono-atomic fe chains on superconducting pb surface. npj Quantum Inf 2:16035
26. Zhang H et al (2018) Quantized Majorana conductance. Nature 556:74
27. Lutchyn RM et al (2018) Majorana zero modes in superconductor-semiconductor heterostructures. Nat Rev Mater 3:52–68
28. Hao N, Hu J (2014) Topological phases in the single-layer FeSe. Phys Rev X 4:031053
29. Wu X, Qin S, Liang Y, Fan H, Hu J (2016) Topological characters in $\mathbf{Fe}(\mathbf{Te}_{1-x}\mathbf{Se}_x)$ thin films. Phys Rev B 93:115129
30. Wang Z et al (2015) Topological nature of the $\mathbf{FeSe}_{0.5}\mathbf{Te}_{0.5}$ superconductor. Phys Rev B 92:115119
31. Xu G, Lian B, Tang P, Qi X-L, Zhang S-C (2016) Topological superconductivity on the surface of Fe-based superconductors. Phys Rev Lett 117:047001
32. Zhang P et al (2018) Observation of topological superconductivity on the surface of an iron-based superconductor. Science 360:182–186
33. Zhang P et al (2019) Multiple topological states in iron-based superconductors. Nat Phys 15:41–47
34. Hao N, Hu J (2018) Topological quantum states of matter in iron-based superconductors: from concept to material realization. Nat Sci Rev 6:213–226
35. Shi X et al (2017) $\mathbf{FeTe}_{1-x}\mathbf{Se}_x$ monolayer films: towards the realization of high-temperature connate topological superconductivity. Sci Bull 62:503–507
36. Peng XL et al (2019) Observation of topological transition in high-T_c superconducting monolayer $\mathbf{FeTe}_{1-x}\mathbf{Se}_x$ films on $\mathbf{SrTiO}_3$(001). Phys Rev B 100:155134
37. Yin JX et al (2015) Observation of a robust zero-energy bound state in iron-based superconductor Fe(Te, Se). Nat Phys 11:543–546
38. Wang D et al (2018) Evidence for Majorana bound states in an iron-based superconductor. Science 362:333–335
39. Liu Q et al (2018) Robust and clean Majorana zero mode in the vortex core of high-temperature superconductor $(\mathbf{Li}_{0.84}\mathbf{Fe}_{0.16})\mathbf{OHFeSe}$. Phys Rev X 8:041056
40. Kong L et al (2019) Half-integer level shift of vortex bound states in an iron-based superconductor. Nat Phys 15:1181–1187
41. Machida T et al (2019) Zero-energy vortex bound state in the superconducting topological surface state of Fe(Se, Te). Nat Mater 18:811–815
42. Liu W et al (2019) A new Majorana platform in an Fe-As bilayer superconductor. arXiv e-prints. arXiv:1907.00904
43. Zhang SS et al (2020) Field-free platform for Majorana-like zero mode in superconductors with a topological surface state. Phys Rev B 101:100507
44. Wang Q, Liu C-C, Lu Y-M, Zhang F (2018) High-temperature Majorana corner states. Phys Rev Lett 121:186801
45. Yan Z, Song F, Wang Z (2018) Majorana corner modes in a high-temperature platform. Phys Rev Lett 121:096803
46. Zhang R-X, Cole WS, Das Sarma S (2019) Interplay between classical magnetic moments and superconductivity in quantum one-dimensional conductors: toward a self-sustained topological Majorana phase. Phys Rev Lett 122:187001
47. Wu X, Liu X, Thomale R, Liu C-X (2022) High-T_c superconductor Fe(Se, Te) monolayer: an intrinsic, scalable and electrically-tunable Majorana platform. Natl Sci Rev 9:nwab087
48. Zhang R-X, Cole WS, Wu X, Das Sarma S (2019) Higher-order topology and nodal topological superconductivity in Fe(Se, Te) heterostructures. Phys Rev Lett 123:167001
49. Wu X et al (2020) Boundary-obstructed topological high-T_c superconductivity in iron pnictides. Phys Rev X 10:041014
50. Chen C et al (2020) Atomic line defects and zero-energy end states in monolayer Fe(Te, Se) high-temperature superconductors. Nat Phys 16:536
51. Ma F, Ji W, Hu J, Lu Z-Y, Xiang T (2009) First-principles calculations of the electronic structure of tetragonal $\boldsymbol{\alpha}$-FeTe and $\boldsymbol{\alpha}$-FeSe crystals: evidence for a bicollinear antiferromagnetic order. Phys Rev Lett 102:177003
52. Zhao W et al (2018) Direct imaging of electron transfer and its influence on superconducting pairing at FeSe/$SrTiO_3$ interface. Sci Adv 4:eaao2682
53. Zhang Y, Jiang K, Zhang F, Wang J, Wang Z (2020) Atomic line defects in unconventional superconductors as a new route toward one dimensional topological superconductors. arXiv e-prints. arXiv:2004.05860
54. Kresse G, Hafner J (1993) Ab initio molecular dynamics for liquid metals. Phys Rev B 47:558–561
55. Kresse G, Furthmüller J (1996) Efficiency of ab-initio total energy calculations for metals and semiconductors using a plane-wave basis set. Comput Mater Sci 6:15–50
56. Kresse G, Furthmüller J (1996) Efficient iterative schemes for ab initio total-energy calculations using a plane-wave basis set. Phys Rev B 54:11169–11186
57. Perdew JP, Burke K, Ernzerhof M (1996) Generalized gradient approximation made simple. Phys Rev Lett 77:3865–3868
58. Monkhorst HJ, Pack JD (1976) Special points for Brillouin-zone integrations. Phys Rev B 13:5188–5192

Publisher's Note